

TIC 322208686: An Eclipsing System with γ Doradus Pulsations and a Third Component on a Wider Orbit

JAE WOO LEE,¹ KYEONGSOO HONG,¹ MIN-JI JEONG,¹ JANG-HO PARK,¹ PAKAKAEW RITTIPRUK,²
AND HYE-YOUNG KIM^{1,3}

¹*Korea Astronomy and Space Science Institute, Daejeon 34055, Republic of Korea*

²*National Astronomical Research Institute of Thailand, Chiang Mai 50200, Thailand*

³*Department of Astronomy and Space Science, Chungbuk National University, Cheongju 28644, Republic of Korea*

ABSTRACT

TIC 322208686 is known to be a detached binary that exhibits two types of variability: pulsation and eclipse. We present the physical properties of the target star using the short-cadence TESS data from sectors 24, 57, and 58, and our echelle spectra that show the presence of a tertiary companion. The spectral analysis led to the triple-lined radial velocities and the atmospheric parameters of the eclipsing components. Joint modeling of these observations reveals that the eclipsing pair contains two F-type stars with masses $1.564 \pm 0.012 M_{\odot}$ and $1.483 \pm 0.012 M_{\odot}$, radii $1.588 \pm 0.011 R_{\odot}$ and $1.500 \pm 0.012 R_{\odot}$, effective temperatures 7028 ± 100 K and 7020 ± 110 K, and luminosities $5.51 \pm 0.32 L_{\odot}$ and $4.90 \pm 0.32 L_{\odot}$. The light contributions of the three stars obtained from this modeling match well with those calculated from the observed spectra. The binary star parameters are in satisfactory agreement with evolutionary model predictions for age $t = 0.4$ Gyr and metallicity $Z = 0.03$. We extracted 11 significant frequencies from the TESS light residuals with the binary effects removed. Of these, five signals between 0.65 day^{-1} and 1.89 day^{-1} can be considered as γ Dor pulsations originating mainly from the primary component, while the other frequencies are likely instrumental artifacts or combination terms. These results suggest that TIC 322208686 is a hierarchical triple, containing a pulsating eclipsing pair and a tertiary companion.

Keywords: Eclipsing binary stars (444) — Spectroscopic binary stars (1557) — Multiple stars (1081) — Fundamental parameters of stars (555) — Stellar pulsations (1625) — Gamma Doradus variable stars (2101) — Stellar evolution (1599)

1. INTRODUCTION

Our knowledge of stellar evolution requires precise measurements of absolute properties such as mass, radius, and effective temperature, which are invaluable in many fields of astrophysics. These measurements are cornerstones for calibrating theoretical evolution models and advancing our understanding of stellar physics. Eclipsing binaries (EBs) serve as the primary source for deriving the physical parameters of their component stars in various stages of evolution. Moreover, they have potential as distance indicators for nearby galaxies of which they are members (R. W. Hilditch 2001; G. Pietrzyński et al. 2013). Orbital solutions that employ different types of observations have significant advantages over those using only one type. For example, combining photometry and spectroscopy allows for accurate determination of fundamental parameters without any assumptions. The absolute masses and radii of detached EBs can be determined with better than 3 % precision through joint modeling of their double-lined radial velocities (RVs) and light curves (J. Andersen 1991; G. Torres et al. 2010). Such EBs are representative of normal stars, as they have not undergone mass transfer. Modern space-based photometric and echelle spectroscopic studies allow measurements of mass and radius of each component with precisions of ~ 0.2 % (e.g., P. F. L. Maxted et al. 2020).

The study of stellar pulsations, known as asteroseismology, can also help improve theoretical models of stars. Comparing the observed pulsation frequencies to theoretical predictions can provide information about the interior physics of stars from core to surface, including their ages, densities, rotational profiles, and chemical compositions, etc (C. Aerts et al. 2010). Therefore, EBs that exhibit oscillating signals are highly valuable due to the synergistic effect of pulsation and binary properties (S. J. Murphy 2018; D. W. Kurtz 2022). Some detached EBs exhibit pulsating features in one or both components (e.g., J. Southworth & T. Van Reeth 2022). Recently, many new pulsating EBs have been discovered through space-based photometric archives such as Kepler and TESS (P. Gaulme & J. A. Guzik 2019; X. Chen et al. 2022; F. Kahraman Aliçavuş et al. 2022; X.-D. Shi et al. 2022; C. I. Eze & G. Handler 2024). However, most of their physical properties remain poorly defined due to lack or absence of spectroscopic data.

This study focuses on the TESS target TIC 322208686 (BD+67 1348, TYC 4462-599-1, 2MASS J21413664+6745394, WISE J2141366+674539, Gaia DR3 2222840880731556736; $T_p = +9.303$), a detached EB with an eclipse period of 1.354 ± 0.005 days discovered by X. Chen et al. (2018) in the WISE data. X.-D. Shi et al. (2022) detected a dominant pulsation with a cycle of 0.79216 ± 0.00004 days and an amplitude of 10.11 ± 0.03 mmag in the EB system, based on 120-s sampling data collected from TESS Sector 24. They reported that the pulsating signal does not follow the relation between the orbital (P_{orb}) and pulsation (P_{pul}) periods of oscillating eclipsing Algols (D. E. Mkrtichian et al. 2004; E. Soyduğan et al. 2006; A. Liakos et al. 2012; X. B. Zhang et al. 2013). Our primary goal here is to accurately determine the absolute properties of the triple-lined EB system with a tertiary companion and multiperiodic pulsations, and to investigate its evolution.

2. TESS PHOTOMETRY AND ECLIPSE TIMINGS

TIC 322208686 was monitored by the TESS satellite (G. R. Ricker et al. 2015) and recorded with 30-min cadence in Sectors 16, 17, and 18 (S16–18; 2019 September 12 to November 27), 120-s cadence in Sector 24 (S24; 2020 April 16 to May 12), and 200-s cadence in Sectors 57 and 58 (S57–58; 2022 September 30 to November 26). In this work, we concentrated on the short-cadence SAP observations of S24 and S57–58 retrieved from the MAST archive¹ for binary modeling and

¹ <https://archive.stsci.edu/>. The TESS data used are accessible at <http://dx.doi.org/10.17909/kzxc-yy89>.

pulsation analysis. Their CROWDSAP parameter is 0.9865 ± 0.0066 on average. The detrending and flux-to-magnitude conversion of the TESS data are identical to those described and applied in [J. W. Lee et al. \(2024\)](#). The resulting time-series observations of TIC 322208686 are displayed in Figure 1, where the observation gap between S24 and S57 is about 871 days. As reported in [X.-D. Shi et al. \(2022\)](#), it is clear that our program target exhibits pulsating signals, especially in outside eclipse phases. We finally secured 18,216 and 21,631 observations in 120-s and 200-s sampling modes, respectively, with a total time span of 954 days.

We measured 92 primary (Min I) and 88 secondary (Min II) minimum epochs of TIC 322208686 from each eclipse curve of the available TESS data, including those with 30-min cadence ([K. K. Kwee & H. Van Woerden 1956](#)). These calculations used at least 8 consecutive observations for each 30-min minimum, and about 100 and 60 observations for 120-s and 200-s minima, respectively. Due to the limited data points, the errors for the 30-min measurements are likely underestimated. In order to obtain the binary’s orbital ephemeris, we applied linear least-squares fitting to them, which resulted in the following ephemeris:

$$\text{Min I} = \text{BJD } 2, 458, 956.38202(20) + 1.35931375(46)E, \quad (1)$$

where the parenthesized numbers are the $1\text{-}\sigma$ errors of the last two digits. The orbital period is slightly shorter and more precisely derived than that (1.35964 ± 0.00032) of [X.-D. Shi et al. \(2022\)](#). The observed TESS eclipse timings are compiled in Table 1, where the third and fourth columns are the cycle numbers and $O - C$ values calculated with equation (1). The $O - C$ diagram of Figure 2 shows that although the mid-eclipse timings of TIC 322208686 are somewhat scattered by its pulsating features, there is a noticeable change in the orbital period. The timing variation may be due to the third object detected spectroscopically in this study. Additionally, the primary and secondary minima are in phase with each other, suggesting that the binary may be in a circular orbit.

3. BOES SPECTROSCOPY AND DATA ANALYSIS

Time-series echelle spectroscopy of TIC 322208686 was performed on 2023 November 12 and 14 at BOAO, Korea. The observations were made using the 1.8-m telescope and the BOES spectrograph ([K.-M. Kim et al. 2007](#)), providing a spectral range from 3600 to 10,200 Å and the resolving power of $\sim 30,000$. A total of 16 optical spectra were acquired with an integration time of 1800 s per frame, which is equivalent to 0.015 of the orbital period, and is therefore unaffected by orbital smearing. In addition, images for pre-processing (bias and Tungsten-Halogen lamp) and wavelength calibration (Th-Ar lamp) were collected before and after these target spectra. The observed BOES spectra were reduced with the `echelle` package of the IRAF software with the standard procedures such as spectral extraction, wavelength calibration, and normalization by continuum. Their signal-to-noise ratios (SNR) were found to be about 30 at a wavelength of around 5000 Å.

The observed spectra of TIC 322208686 clearly show the three absorption lines originating from the eclipsing components and an additional object. The sample spectra in the H_β region, presented in the left panel of Figure 3, demonstrate that the absorption lines of the close pair AB are shifted due to the Doppler effect, while those of the third spectroscopic source are unchanged. For the RV measurements of the three components, we adopted the broadening function (BF) technique ([S. M. Rucinski 2002](#)) of the `RaveSpan` software² ([B. Pilecki et al. 2012](#)), which is especially useful when the

² <https://users.camk.edu.pl/pilecki/ravespan/>

spectral lines are blended. The BF method decomposes a target composite spectrum into individual stars using a sharp-lined template, maintains higher resolution compared to the cross-correlation technique, and makes it easier to determine the light contribution by simple integration. In this way, it enables the identification of faint companions (e.g., [J. W. Lee et al. 2024](#)).

In this process, the template spectrum was taken from the model library of synthetic spectra by [P. Coelho et al. \(2005\)](#). The spectral region from 4840 to 5385 Å containing H β and Mg I b triplet at 5167, 5172, and 5183 Å was selected for the BF work, where no significant telluric lines were observed. We measured the RVs applying the rotational function to each BF profile. As samples, the BF profiles for two orbital phases are illustrated with the fitted rotational profiles in the right panels of [Figure 3](#). The RV measurement results for this triple are summarized in [Table 2](#) and displayed in [Figure 4](#). In this figure, the RVs of the eclipsing pair vary with its orbital motion, while those of the tertiary companion remain almost constant at the average RV of -13.86 ± 0.37 km s $^{-1}$. The light contributions of individual components, $l/(l_A + l_B + l_C)$, estimated from the BF profiles are on average 44 %, 40 %, and 16 % for the primary, secondary, and tertiary stars, respectively ([S. M. Rucinski & T. Pribulla 2008](#); [J. W. Lee et al. 2024](#)). These values are intensity ratios of the spectral lines used in the BF and therefore do not directly constrain the continuum or overall light contributions.

To measure the components' atmospheric parameters, the observed spectra were disentangled using the `DISENTANGLING_SHIFT_AND_ADD` code³ ([T. Shenar et al. 2020, 2022](#)) over the wavelength range of 3800–5080 Å, which includes the temperature indicators of H $_9$, H $_8$, Ca II K, H $_\epsilon$, H $_\delta$, H $_\gamma$, and H $_\beta$. The initial parameters for the disentangling procedure, such as orbital ephemeris (T_0 , P_{orb}), eccentricity (e), and RV semi-amplitudes (K_1 , K_2), were obtained from the binary modeling in the following section. Unfortunately, the disentangled spectrum of the third component could not be extracted due to insufficient information about its orbital parameters. After running this procedure, the disentangled spectra of the primary and secondary stars were normalized using the `SUPPNET` package⁴ ([T. Rózański et al. 2022](#)).

Using the `GSSP` software package⁵ ([A. Tkachenko 2015](#)), each disentangled spectrum was compared with synthetic spectra computed using the radiative transfer code `SYNTHV` ([V. Tsymbal 1996](#)) and a grid of `LLMODELS` stellar atmosphere models ([D. Shulyak et al. 2004](#)). The *TESS* v8.2 ([M. Paegert et al. 2022](#)) and *Gaia* DR3 ([Gaia Collaboration et al. 2023](#)) catalogues reported the effective temperature (T_{eff}) of TIC 322208686 as 7043 ± 192 K and 6731_{-18}^{+16} K, respectively, so we used these as starting values. The surface gravities of the eclipsing components were set to $\log g_{A,B} = 4.2$ from our modeling results. The micro- and macro-turbulence velocities were estimated by applying T_{eff} , $\log g$, and metallicities $[M/H]$ to empirical relationships built in the `iSpec` code⁶ ([S. Blanco-Cuaresma et al. 2014](#)).

In the `GSSP` runs, the effective temperature, rotational velocity, and metallicity were adjusted and evaluated. However, we could not determine the metallicities of both components, probably due to low SNR and the incompleteness of the disentangled spectra. Therefore, the analysis proceeded in two steps. In the first step, we used the solar metallicities for each star. In the second step, the metallicities were set to $[M/H] = 0.3$, as inferred from the comparisons with evolutionary models described in the last section. As a result of this run, the effective temperatures and rotational

³ https://github.com/TomerShenar/Disentangling_Shift_And_Add/

⁴ <https://github.com/RozanskiT/suppnet/>

⁵ <https://fys.kuleuven.be/ster/meetings/binary-2015/gssp-software-package>

⁶ <https://www.blancocuaresma.com/s/iSpec/>

velocities were found to be optimal at $T_{A,\text{eff}} = 7028 \pm 100$ K and $v_A \sin i = 76 \pm 6$ km s⁻¹ for the primary component, and at $T_{B,\text{eff}} = 6904 \pm 210$ K and $v_B \sin i = 64 \pm 6$ km s⁻¹ for the secondary component, by fitting a polynomial to the lowest χ^2 values (cf. [H. Lehmann et al. 2011](#)). The micro- and macro-turbulence velocities were obtained as 1.77 km s⁻¹ and 14.65 km s⁻¹ for TIC 322208686 A, and 1.69 km s⁻¹ and 13.08 km s⁻¹ for its companion, respectively. Figure 5 shows the disentangled and best-fit spectra of the primary and secondary components.

4. BINARY MODELING AND ABSOLUTE PARAMETERS

Observing double-lined EBs provides a unique opportunity to directly and precisely measure their most fundamental parameters, such as masses and radii. Such measurements will help to constrain and better understand models of stellar structure and evolution. The TESS photometric and BOES spectroscopic observations reveal that TIC 322208686 is a triple-lined RV system exhibiting continuous and significant brightness variations due to multiple pulsations. In addition, the phase difference between Min I and Min II is around 0.50, and the $O - C$ diagram of the eclipse timings in Figure 2 shows that the two eclipse types are in phase with each other. These imply that the orbital eccentricity of the inner binary is nearly zero. The Wilson-Devinney (W-D) modeling code ([R. E. Wilson & E. J. Devinney 1971](#); [J. Kallrath 2022](#)) was adopted to compute our target star observables. Our RV measurements were modeled with the short-cadence TESS light curves (S24, S57, and S58) in the same way as for the hierarchical triple WASP 0346-21 ([J. W. Lee et al. 2024](#)).

For this modeling, the primary’s temperature was fixed to $T_{A,\text{eff}} = 7028 \pm 100$ K as measured from the BOES spectra, while the secondary’s $T_{B,\text{eff}}$ was adjusted to best fit the ultra-precise light curves. We set the rotation parameters of the eclipsing components to $F_A = 1.33 \pm 0.11$ and $F_B = 1.18 \pm 0.11$ from the ratio of the observed $v_{\text{obs}} \approx v \sin i$ and the calculated synchronous rotation v_{sync} . The limb-darkening parameters $x_{A,B}$ and $y_{A,B}$ for the logarithmic law were interpolated from the updated values of [W. Van Hamme \(1993\)](#) implemented in the W-D code. Since the public TESS photometry and our BOES spectroscopy were not performed simultaneously and the tertiary object was detected in the echelle spectra but its orbital parameters are unknown, these two types of datasets were solved separately and iteratively ([J. W. Lee et al. 2024, 2025](#)).

The fitted parameters in the W-D run are: for the light curves, orbital ephemeris T_0 and P_{orb} , inclination angle i , secondary’s temperature $T_{B,\text{eff}}$, dimensionless surface potentials $\Omega_{A,B}$, and bandpass luminosities l_A and l_B ; and for the RV curves, reference epoch T_0 , orbital semi-major axis a , systemic velocity γ , and mass ratio q . The resulting parameters from the binary modeling are presented in Table 3, and the corresponding model fits are superimposed on the observed light and RV curves as gray and red solid lines in Figures 1 and 4, respectively. In addition, the phase-folded light curve and the W-D model residuals are shown in Figure 6. The agreement between the binary model and the observations is very good. To yield the parameter errors in Table 3, we applied numerous models with different inputs of the initial parameters and various approaches. From these runs, we estimated the errors using the variation in each fitted parameter ([J. Southworth & D. M. Bowman 2022](#)).

As presented in the next section, our target star exhibited multiperiod pulsations, so we investigated whether they affected the binary parameters. First, we found the pulsating frequencies from all residual lights, including the data of both eclipse phases. We then analyzed the pre-whitened EB light curve, removing these pulsations, using the W-D code. The results are in good agreement with those from observed TESS data within their errors. The absolute properties of TIC 322208686 were computed using the parameters in Table 3 obtained from the joint light and RV fits. We assigned the

solar temperature and bolometric magnitude as $T_{\text{eff}\odot} = 5780$ K and $M_{\text{bol}\odot} = +4.73$, respectively. The calculation results are summarized in Table 4, where the bolometric corrections (BC) were adopted from empirical relationships with the effective temperatures of the component stars (P. J. Flower 1996; G. Torres 2010).

The distance to an EB system is usually calculated via the distance-modulus equation $V - A_V - M_V = 5 \log d - 5$, with the apparent magnitude V taken at maximum light and the interstellar extinction $A_V \simeq 3.1E(B - V)$. For our target TIC 322208686, the TESS v8.2 catalogue (M. Paegert et al. 2022) gave $V = +9.685 \pm 0.004$, $(B - V) = +0.372 \pm 0.051$, and $E(B - V) = 0.054 \pm 0.028$. The TESS V magnitude would be the combined brightness of the triple system, including the third companion detected in this study. Assuming that the third-light contribution derived from our TESS modelling and the BFs approximately reflects the V -band contribution, we calculated an apparent magnitude of $V_{\text{EB}} = 9.870$ for the eclipsing pair of TIC 322208686. Using V_{EB} , the TESS color index, and our modeling parameters in Tables 3 and 4, we estimated a geometric distance of $d = 323 \pm 13$ pc for TIC 322208686 AB, which is 53 ± 14 pc closer than 376 ± 6 pc inverted from the Gaia DR3 parallax of $\pi = 2.661 \pm 0.041$ mas (Gaia Collaboration et al. 2023). Ignoring interstellar reddening ($A_V = 0.0$), the EB distance increases to 349 ± 14 pc, but is still smaller than the GAIA distance. The discrepancy between the EB and GAIA distances may be partly attributable to brightness variations caused by pulsations.

The Gaia parameter RUWE indicates the goodness-of-fit of the astrometric solution for this spacecraft and is quite sensitive to unresolved close companions (K. G. Stassun & G. Torres 2021). TIC 322208686 has a RUWE value of 3.181, which is considerably larger than the good solution of $\lesssim 1.0$. RUWE values higher than 1.4 indicate that the astrometric fits are unreliable and do not perfectly describe the motion of the objects. This may be caused by the presence of the tight tertiaries in binary systems. The unusual RUWE value in TIC 322208686 may be due to a third companion star detected in our BOES spectrum.

5. PULSATIONAL CHARACTERISTICS

The fundamental parameters in Table 4 indicate that the eclipsing components are main-sequence dwarfs with spectral type \sim F1 V and are therefore candidates for intermediate-mass pulsators such as γ Dor or δ Sct variables (V. Antoci et al. 2019). Figure 7 presents the TESS light residuals of the W-D model fit, with the lower panel providing more details on the residuals. This figure shows distinct brightness variations with a main period of about 0.80 days and a maximum amplitude of > 20 mmag. To reliably extract the pulsation signals, we used the out-of-eclipse residuals with the binary effects removed. The frequency search was conducted using the PERIOD04 computer code (P. Lenz & M. Breger 2005) up to the Nyquist frequency $f_{\text{Ny}} = 216 \text{ day}^{-1}$, which corresponds to a sampling rate of 200 s for S57 and S58. We first analyzed each of two datasets, S24 and S57–58, separated by a long observation gap of more than 2 yrs. The resultant amplitude spectra are presented in the first and second panels of Figure 8. There are no noticeable difference in amplitudes or frequencies between them.

Our frequency analysis was finally applied to the full short-cadence residuals, excluding the two eclipse periods, to find consistent pulsation signals. As a consequence, we extracted 11 significant frequencies with SNR greater than 5 (A. S. Baran & C. Koen 2021; J. W. Lee et al. 2025) using an iterative pre-whitening method. In this process, the residual light curves were pre-whitened to the next frequency after finding the frequency (J. W. Lee et al. 2014). The third and bottom panels of

Figure 8 display the Fourier amplitude spectra for the three sectors’ residuals, respectively, with the most dominant f_1 frequency and all 11 frequencies pre-whitened. We did not find any significant signals in the frequency range of $> 5 \text{ day}^{-1}$, which is not displayed in this figure.

The multi-frequency parameters for TIC 322208686 are summarized in Table 5, and the resulting synthetic curve is plotted as a red solid line in the lower panel of Figure 7. The residual light curves from the 11-frequency fit, with both binary and pulsation effects removed, are offset by +20 mmag and appear as blue dots on the same panel. This figure reveals that the in-eclipse residuals deviate from the general trend of the outside-eclipse residuals. During the primary eclipses, the residual light curves get darker until conjunctions and then brighten again, whereas during the secondary eclipses, the reverse occurs: they brighten to conjunctions and then darken. These features suggest that the light contribution from pulsations to the EB system is relatively largest at the secondary minimum among the entire binary orbit, and thus the primary star maximally obscuring the secondary companion at Min II is a pulsating variable.

In order to uncover aliasing signals such as frequency harmonic and combination terms, the assigned frequency resolution F_{res} was $1.5/\Delta T = 0.00157 \text{ day}^{-1}$ using the duration $\Delta T = 954.3$ days of the TESS data used (G. L. Loumos & T. J. Deeming 1978). The search results are presented on the remark column in Table 5. Within the F_{res} criterion, frequencies f_3 , f_6 , and f_9 are combinations with the detected signals and/or orbital frequency ($f_{\text{orb}} = 0.73566 \text{ day}^{-1}$), while f_5 is twice the most prominent frequency f_1 . Also, the lowest frequencies f_7 and f_{10} appear to be artifacts related to the 13.7-day TESS orbit. The remaining frequencies can be considered independent signals, and their pulsation constants were obtained from the relationship $Q_i = f_i \sqrt{\rho_A/\rho_\odot}$, as follows: $Q_1 = 0.496$ days, $Q_2 = 0.847$ days, $Q_4 = 0.542$ days, $Q_8 = 0.951$ days, and $Q_{11} = 0.332$ days. The pulsation frequencies and Q values are within the typical ranges of γ Dor variables (A. Grigahcène et al. 2010; K. Uytterhoeven et al. 2011). The frequency ratio of $f_{\text{orb}}:f_1 \simeq 3:5$ suggests that the dominant γ Dor pulsation may arise from tidal interactions between the EB components.

6. DISCUSSION AND CONCLUSION

In this study, we present the first-measured spectroscopic characterizations of TIC 322208686 with high-quality TESS data. The BOES echelle spectra showed the presence of not only the eclipsing pair but also a tertiary companion. We obtained the RV measurements of the three objects using the BF profiles with rotation functions applied. While the eclipsing components moved with similar RV semi-amplitudes ($K_{A,B}$) in a 1.3593-day circular orbit, the tertiary object showed little change during the observation run, with an average velocity of $-13.86 \pm 0.37 \text{ km s}^{-1}$. The disentangled spectra for each EB component were extracted using the `DISENTANGLING_SHIFT_AND_ADD` code, and compared to synthetic model grids to determine the effective temperatures and rotational rates for solar metallicity and $[M/H] = 0.3$. The spectral analyses revealed that TIC 322208686 is a triple-lined star system consisting of an inner F1 V pair and a distant tertiary.

We synthesized the TESS light and our RV curves of the triple system, including the atmospheric parameters, to characterize its physical properties of $M_A = 1.564 \pm 0.012 M_\odot$, $R_A = 1.588 \pm 0.011 R_\odot$, $T_{A,\text{eff}} = 7028 \pm 100 \text{ K}$, and $L_A = 5.51 \pm 0.32 L_\odot$ for TIC 322208686 A and $M_B = 1.483 \pm 0.012 M_\odot$, $R_B = 1.500 \pm 0.012 R_\odot$, $T_{B,\text{eff}} = 7020 \pm 110 \text{ K}$, and $L_B = 4.90 \pm 0.32 L_\odot$ for TIC 322208686 B, respectively. The binary modeling allowed us to derive the masses and radii of the eclipsing pair to less than 1 % accuracy. Our measurements of $v_{A,B} \sin i$ indicate that the eclipsing components A and B are expected to be in a state of supersynchronization at present. The light fractions of the

three components, calculated via this synthesis, agree well with the average values obtained from the BOES spectra.

Comparisons of the EB fundamental parameters with stellar models provide a straightforward and clear interpretation of the agreement between observations and theory. In particular, since mass, radius, and temperature are physical properties that can be measured directly through observations, one of the most effective methods would be to compare them to the model predictions. To study the evolutionary status of TIC 322208686, we first plotted the positions of the EB components on the mass-radius ($M - R$) and mass-temperature ($M - T_{\text{eff}}$) diagrams in the left panels of Figure 9. Here, the dotted, solid, and dashed lines are the PARSEC v1.2S stellar evolution models⁷ (A. Bressan et al. 2012) with metal abundances Z of 0.017 (solar value), 0.03, and 0.04, respectively. We found an acceptable fit for a model with an age of $t = 0.4$ Gyr and a metallicity of $Z = 0.03$, which is more metal-rich than the solar composition used in our initial spectral analysis. Our choice of age and metallicity is further supported by the $T_{\text{eff}} - L$ plot in the right panel of Figure 9. The cyan and red solid lines denote the zero-age main sequence (ZAMS) and the 0.4-Gyr isochrone, both with $Z = 0.03$. In the H-R diagram, the A component is slightly evolved from ZAMS, while the B companion, which is about $0.08 M_{\odot}$ lighter, is located on ZAMS.

For Galactic kinematics and population membership, we calculated the space velocities of TIC 322208686 as $U = 27.8 \pm 0.7 \text{ km s}^{-1}$, $V = 235.6 \pm 0.7 \text{ km s}^{-1}$, and $W = -1.1 \pm 0.3 \text{ km s}^{-1}$, using the same approach as for J. W. Lee et al. (2024) based on the formulation of D. R. H. Johnson & D. R. Soderblom (1987). In this calculation, we used the Gaia DR3 measurements and our γ velocity and distance. The EB position in the $U - V$ diagram suggests that the target star has the kinematics of the thin-disk population (E.-M. Pauli et al. 2006). The classification of TIC 322208686 as a thin-disk star is consistent with the metallicity of $Z = 0.03$ predicted by stellar evolution models.

¹ This paper is based on the echelle spectra obtained from BOAO and the light curves made by the
² TESS mission. The short-cadence TESS data were collected through Guest Investigator Program
³ G022208 (PI: Nadia Zakamska). We wish to thank the valuable comments and suggestions of the
⁴ anonymous referee. We gratefully acknowledge the support by the KASI grant 2025-1-830-05. H.-
⁵ Y.K. was supported by the grant number RS-2023-00271900 from the National Research Foundation
⁶ (NRF) of Korea.

⁷ <https://stev.oapd.inaf.it/PARSEC/>

REFERENCES

- Aerts, C., Christensen-Dalsgaard, J., & Kurtz, D. W. 2010, *Asteroseismology* (Dordrecht: Springer), doi: [10.1007/978-1-4020-5803-5](https://doi.org/10.1007/978-1-4020-5803-5)
- Andersen, J. 1991, *A&AR*, 3, 91, doi: [10.1007/BF00873538](https://doi.org/10.1007/BF00873538)
- Antoci, V., Cunha, M. S., Bowman, D. M., et al. 2019, *MNRAS*, 490, 4040, doi: [10.1093/mnras/stz2787](https://doi.org/10.1093/mnras/stz2787)
- Baran, A. S., & Koen, C. 2021, *AcA*, 71, 113, doi: [10.32023/0001-5237/71.2.3](https://doi.org/10.32023/0001-5237/71.2.3)
- Blanco-Cuaresma, S., Soubiran, C., Heiter, U., et al. 2014, *A&A*, 569, A111, doi: [10.1051/0004-6361/201423945](https://doi.org/10.1051/0004-6361/201423945)
- Bressan, A., Marigo, P., Girardi, L., et al. 2012, *MNRAS*, 427, 127, doi: [10.1111/j.1365-2966.2012.21948.x](https://doi.org/10.1111/j.1365-2966.2012.21948.x)
- Chen, X., Ding, X., Cheng, L., et al. 2022, *ApJS*, 263, 34, doi: [10.3847/1538-4365/aca284](https://doi.org/10.3847/1538-4365/aca284)
- Chen, X., Wang, S., Deng, L., de Grijs, R., & Yang, M. 2018, *ApJS*, 237, 28, doi: [10.3847/1538-4365/aad32b](https://doi.org/10.3847/1538-4365/aad32b)
- Coelho, P., Barbuy, B., Melendez, J., Sciavon, R. P., & Castilho, B. V. 2005, *A&A*, 443, 735, doi: [10.1051/0004-6361:20053511](https://doi.org/10.1051/0004-6361:20053511)
- Eze, C. I., & Handler, G. 2024, *ApJS*, 272, 25, doi: [10.3847/1538-4365/ad39c5](https://doi.org/10.3847/1538-4365/ad39c5)
- Flower, P. J. 1996, *ApJ*, 469, 355, doi: [10.1086/177785](https://doi.org/10.1086/177785)
- Gaia Collaboration, Vallenari A., Brown A. G. A., et al. 2023, *A&A*, 674, A1, doi: [10.1051/0004-6361/202243940](https://doi.org/10.1051/0004-6361/202243940)
- Gaulme, P., & Guzik, J. A. 2019, *A&A*, 630, A106, doi: [10.1051/0004-6361/201935821](https://doi.org/10.1051/0004-6361/201935821)
- Grigahcène, A., Antoci, V., Balona, L., et al. 2010, *ApJ*, 713, L192, doi: [10.1088/2041-8205/713/2/L192](https://doi.org/10.1088/2041-8205/713/2/L192)
- Hilditch, R. W. 2001, *An Introduction to Close Binary Stars* (Cambridge: Cambridge Univ. Press)
- Johnson, D. R. H., & Soderblom, D. R. 1987, *AJ*, 93, 864, doi: [10.1086/114370](https://doi.org/10.1086/114370)
- Kahraman Aliçavuş, F., Gümüş, D., Kirmizitaş, Ö., et al. 2022, *RAA*, 22, 085003, doi: [10.1088/1674-4527/ac71a4](https://doi.org/10.1088/1674-4527/ac71a4)
- Kallinger, T., Reegen, P., & Weiss, W. W. 2008, *A&A*, 481, 571, doi: [10.1051/0004-6361:20077559](https://doi.org/10.1051/0004-6361:20077559)
- Kallrath, J. 2022, *Galaxies*, 10, 17, doi: [10.3390/galaxies10010017](https://doi.org/10.3390/galaxies10010017)
- Kim, K.-M., Han, I., Valyavin, G. G., et al. 2007, *PASP*, 119, 1052, doi: [doi:10.1086/521959](https://doi.org/10.1086/521959)
- Kurtz, D. W. 2022, *ARAA*, 60, 31, doi: [10.1146/annurev-astro-052920-094232](https://doi.org/10.1146/annurev-astro-052920-094232)
- Kwee, K. K., & Van Woerden, H. 1956, *Bull. Astron. Inst. Netherlands*, 12, 327
- Lee, J. W., Hong, K., Jeong, M.-J., & Wolf, M. 2024, *ApJ*, 973, 113, doi: [10.3847/1538-4357/ad67c7](https://doi.org/10.3847/1538-4357/ad67c7)
- Lee, J. W., Jeong, M.-J., & Hong, K. 2025, *MNRAS*, 538, 3314, doi: [10.1093/mnras/staf473](https://doi.org/10.1093/mnras/staf473)
- Lee, J. W., Kim, S.-L., Hong, K., Lee, C.-U., & Koo, J.-R. 2014, *AJ*, 148, 37, doi: [10.1088/0004-6256/148/2/37](https://doi.org/10.1088/0004-6256/148/2/37)
- Lehmann, H., Tkachenko, A., Semaan, T., et al. 2011, *A&A*, 526, A124, doi: [10.1051/0004-6361/201015769](https://doi.org/10.1051/0004-6361/201015769)
- Lenz, P., & Breger, M. 2005, *Comm. Asteroseismology*, 146, 53, doi: [10.1553/cia146s53](https://doi.org/10.1553/cia146s53)
- Liakos, A., Niarchos, P., Soyduğan, E., et al. 2012, *MNRAS*, 422, 1250, doi: [10.1111/j.1365-2966.2012.20704.x](https://doi.org/10.1111/j.1365-2966.2012.20704.x)
- Loumos, G. L., & Deeming T. J. 1978, *Ap&SS*, 56, 285, doi: [10.1007/BF01879560](https://doi.org/10.1007/BF01879560)
- Maxted, P. F. L., Gaulme, P., Graczyk, D., et al. 2020, *MNRAS*, 498, 332, doi: [10.1093/mnras/staa1662](https://doi.org/10.1093/mnras/staa1662)
- Mkrtichian, D. E., Kusakin, A. V., Rodriguez, E., et al. 2004, *A&A*, 419, 1015, doi: [10.1051/0004-6361:20040095](https://doi.org/10.1051/0004-6361:20040095)
- Murphy, S. J. 2018, arXiv e-prints, <https://arxiv.org/abs/arXiv:1811.12659>
- Paegert, M., Stassun, K. G., Collins, K. A., et al. 2022, *VizieR Online Data Catalog*, IV/39
- Pauli, E.-M., Napiwotzki, R., Heber, U., Altmann, M., & Odenkirchen, M. 2006, *A&A*, 447, 173, doi: [10.1051/0004-6361:20052730](https://doi.org/10.1051/0004-6361:20052730)
- Pietrzyński, G., Graczyk, D., Gieren, W., et al. 2013, *Nature*, 495, 76, doi: [10.1038/nature11878](https://doi.org/10.1038/nature11878)
- Pilecki, B., Konorski, P., & Gorski, M. 2012, in *IAU Symp. 282, From Interacting Binaries to Exoplanets: Essential Modeling Tools*, ed. M. T. Richards, & I. Hubeny (Cambridge: Cambridge Univ. Press), 301, doi: [10.1017/S174392131102761X](https://doi.org/10.1017/S174392131102761X)

- Ricker, G. R., Winn, J. N., Vanderspek, R., et al. 2015, *JATIS*, 1, 014003, doi: [10.1117/1.JATIS.1.1.014003](https://doi.org/10.1117/1.JATIS.1.1.014003)
- Rózański, T., Niemczura, E., Lemiesz, J., et al. 2022, *A&A*, 659, A199, doi: [10.1051/0004-6361/202141480](https://doi.org/10.1051/0004-6361/202141480)
- Rucinski, S. M. 2002, *AJ*, 124, 1746, doi: [10.1086/342342](https://doi.org/10.1086/342342)
- Rucinski, S. M., & Pribulla, T. 2008, *MNRAS*, 388, 1831, doi: [10.1111/j.1365-2966.2008.13508.x](https://doi.org/10.1111/j.1365-2966.2008.13508.x)
- Shenar, T., Bodensteiner, J., Abdul-Masih, M., et al. 2020, *A&A*, 639, L6, doi: [10.1051/0004-6361/202038275](https://doi.org/10.1051/0004-6361/202038275)
- Shenar, T., Sana, H., Mahy, L., et al. 2022, *A&A*, 665, A148, doi: [10.1051/0004-6361/202244245](https://doi.org/10.1051/0004-6361/202244245)
- Shi, X.-D., Qian, S.-B., & Li, L.-J. 2022, *ApJS*, 259, 50, doi: [10.3847/1538-4365/ac59b9](https://doi.org/10.3847/1538-4365/ac59b9)
- Shulyak, D., Tsymbal, V., Ryabchikova, T., et al. 2004, *A&A*, 428, 993, doi: [10.1051/0004-6361:20034169](https://doi.org/10.1051/0004-6361:20034169)
- Southworth, J., & Bowman, D. M. 2022, *The Observatory*, 142, 161, doi: [10.48550/arXiv.2205.08841](https://doi.org/10.48550/arXiv.2205.08841)
- Southworth, J., & Van Reeth, T. 2022, *MNRAS*, 515, 2755, doi: [10.1093/mnras/stac1993](https://doi.org/10.1093/mnras/stac1993)
- Soydugan, E., İbanoglu, C., Soydugan, F., Akan, M. C., & Demircan, O. 2006, *MNRAS*, 366, 1298, doi: [10.1111/j.1365-2966.2005.09889.x](https://doi.org/10.1111/j.1365-2966.2005.09889.x)
- Stassun, K. G., & Torres, G. 2021, *ApJL*, 907, L33, doi: [10.3847/2041-8213/abdaad](https://doi.org/10.3847/2041-8213/abdaad)
- Tkachenko, A. 2015, *A&A*, 581, A129, doi: [10.1051/0004-6361/201526513](https://doi.org/10.1051/0004-6361/201526513)
- Torres, G. 2010, *AJ*, 140, 1158, doi: [10.1088/0004-6256/140/5/1158](https://doi.org/10.1088/0004-6256/140/5/1158)
- Torres, G., Andersen, J., & Giménez, A. 2010, *A&AR*, 18, 67, doi: [10.1007/s00159-009-0025-1](https://doi.org/10.1007/s00159-009-0025-1)
- Tsymbal, V. 1996, in *ASP Conf. Ser.* 108, M.A.S.S., Model Atmospheres and Spectrum Synthesis, ed. S. J. Adelman, F. Kupka, & W. W. Weiss (San Francisco, CA: ASP), 198
- Uytterhoeven, K., Moya, A., Grigahcène, A., et al. 2011, *A&A*, 534, A12, doi: [10.1051/0004-6361/201117368](https://doi.org/10.1051/0004-6361/201117368)
- Van Hamme, W. 1993, *AJ*, 106, 209, doi: [10.1086/116788](https://doi.org/10.1086/116788)
- Wilson, R. E., & Devinney, E. J. 1971, *ApJ*, 166, 605, doi: [10.1086/150986](https://doi.org/10.1086/150986)
- Zhang, X. B., Luo, C. Q., & Fu, J. N. 2013, *ApJ*, 777, 77, doi: [10.1088/0004-637X/777/1/77](https://doi.org/10.1088/0004-637X/777/1/77)

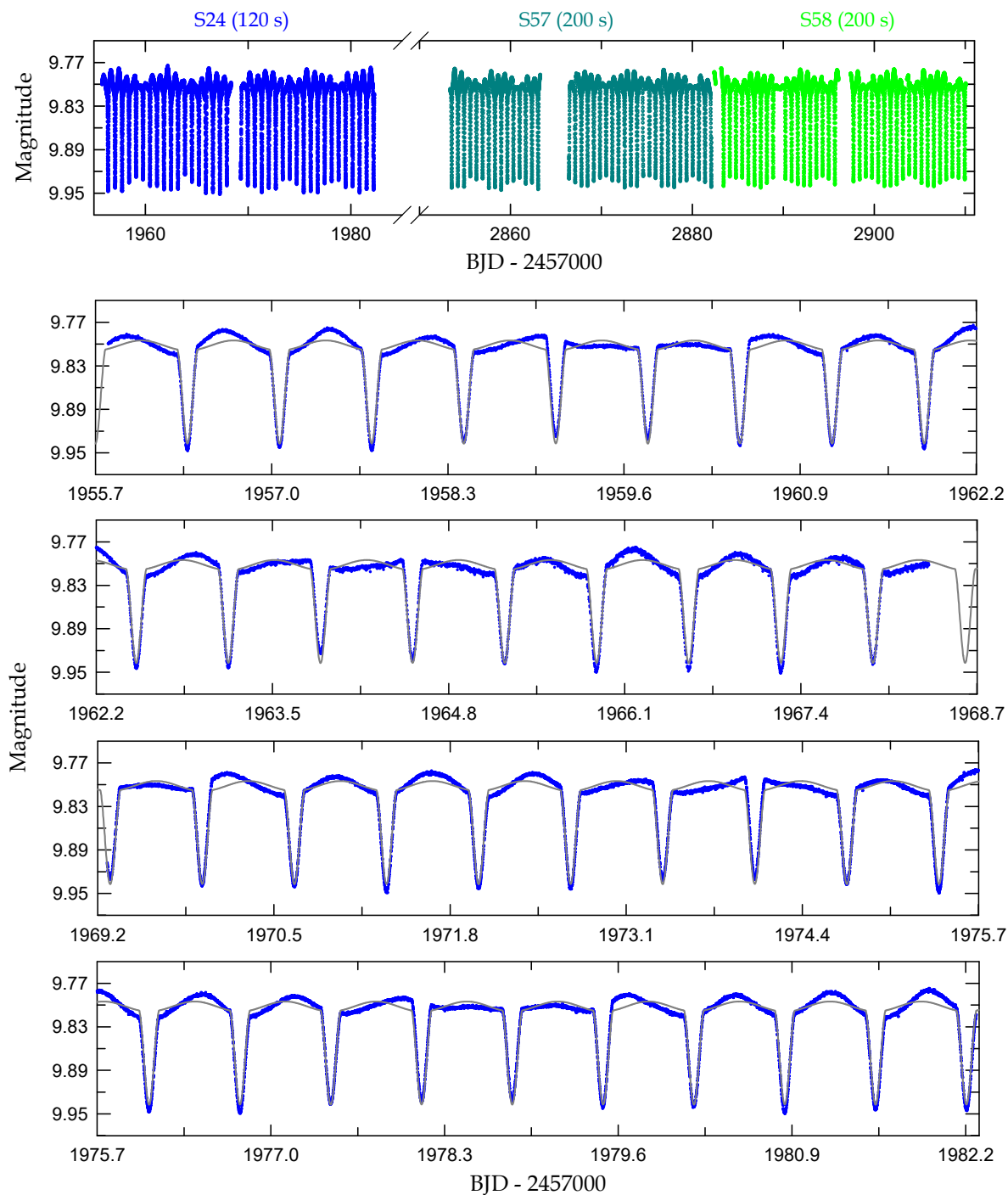


Figure 1. Time-series TESS data of TIC 322208686 observed during Sectors 24 (blue), 57 (cyan), and 58 (green). The top panel shows all observations from the three sectors, and the other panels detail 120-s cadence measurements from Sector 24. The gray lines represent the synthetic model curves computed from our binary star parameters in Table 3.

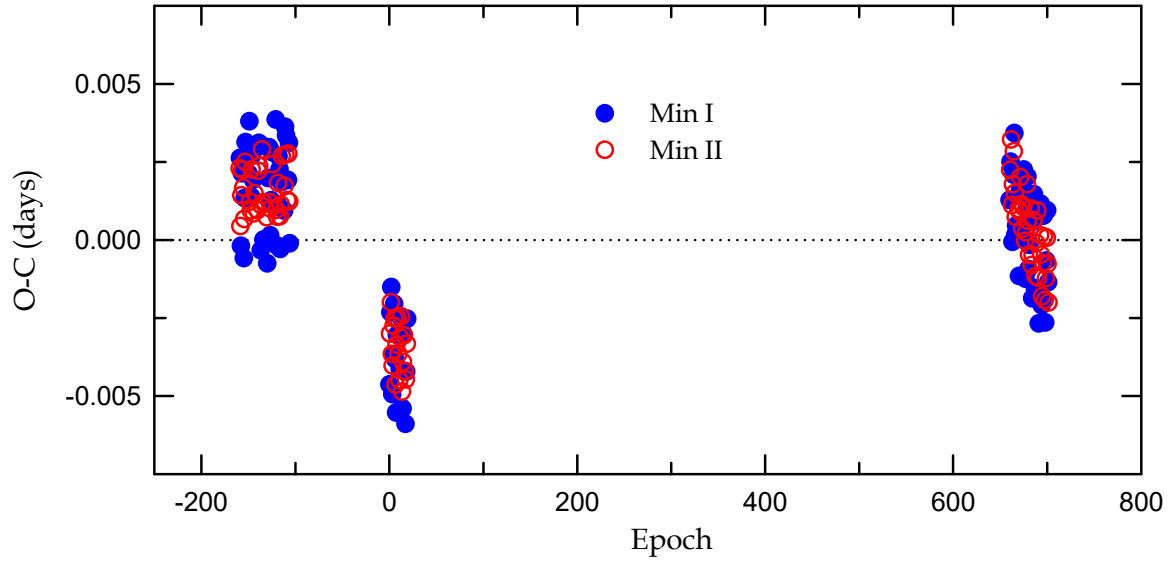


Figure 2. Eclipse timing $O-C$ residuals for TIC 322208686 constructed with the orbital ephemeris (1). The filled and open circles represent the times of the primary and secondary eclipses, labeled Min I and Min II, respectively.

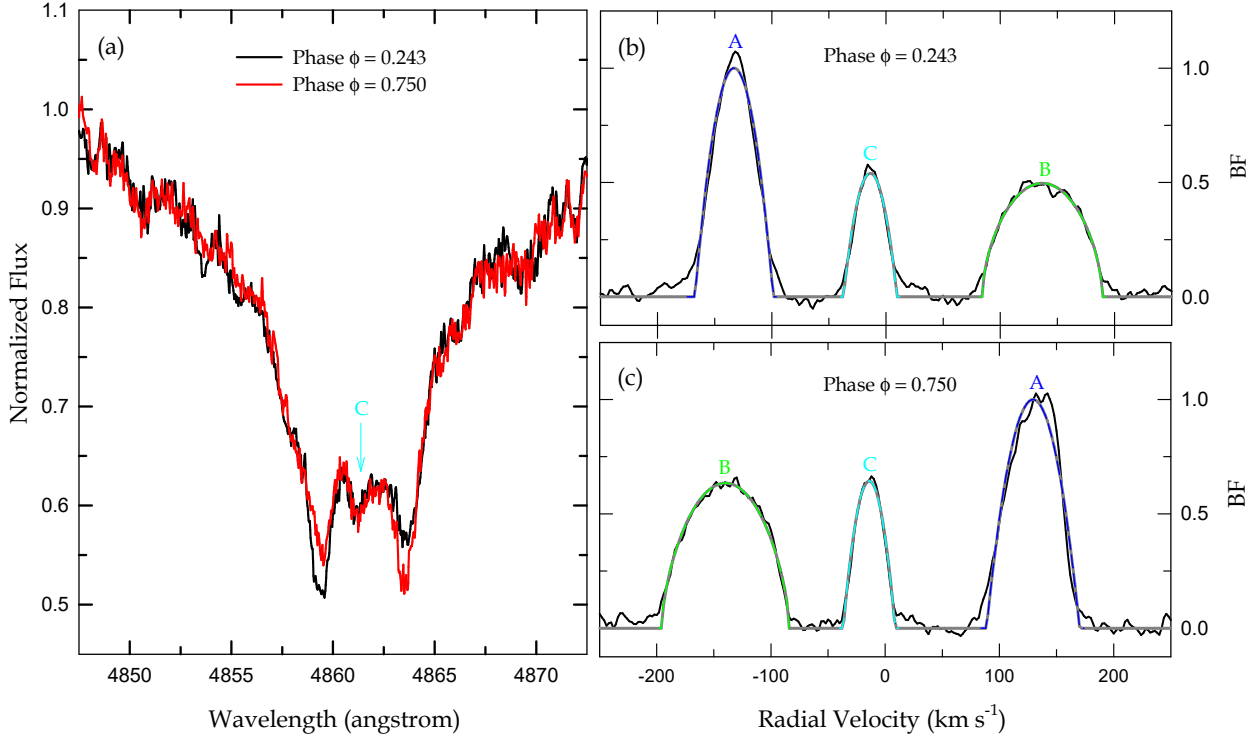


Figure 3. Left panel (a): H_{β} -region spectra observed at orbital phases $\phi = 0.243$ (BJD 2,460,263.0198) and $\phi = 0.750$ (BJD 2,460,260.9902). The signature of the tertiary companion, indicated by an arrow, is well defined between the two absorptions of the eclipsing pair AB. Right panels (b) and (c): BF profiles for the same phases as before obtained using the `RaveSpan` code. The solid black lines indicate the BF profiles, which exhibit triple peaks and are fitted with three rotational profile functions representing the primary (blue), secondary (green), and third (cyan) components. The gray lines correspond to the combination of these rotational profiles.

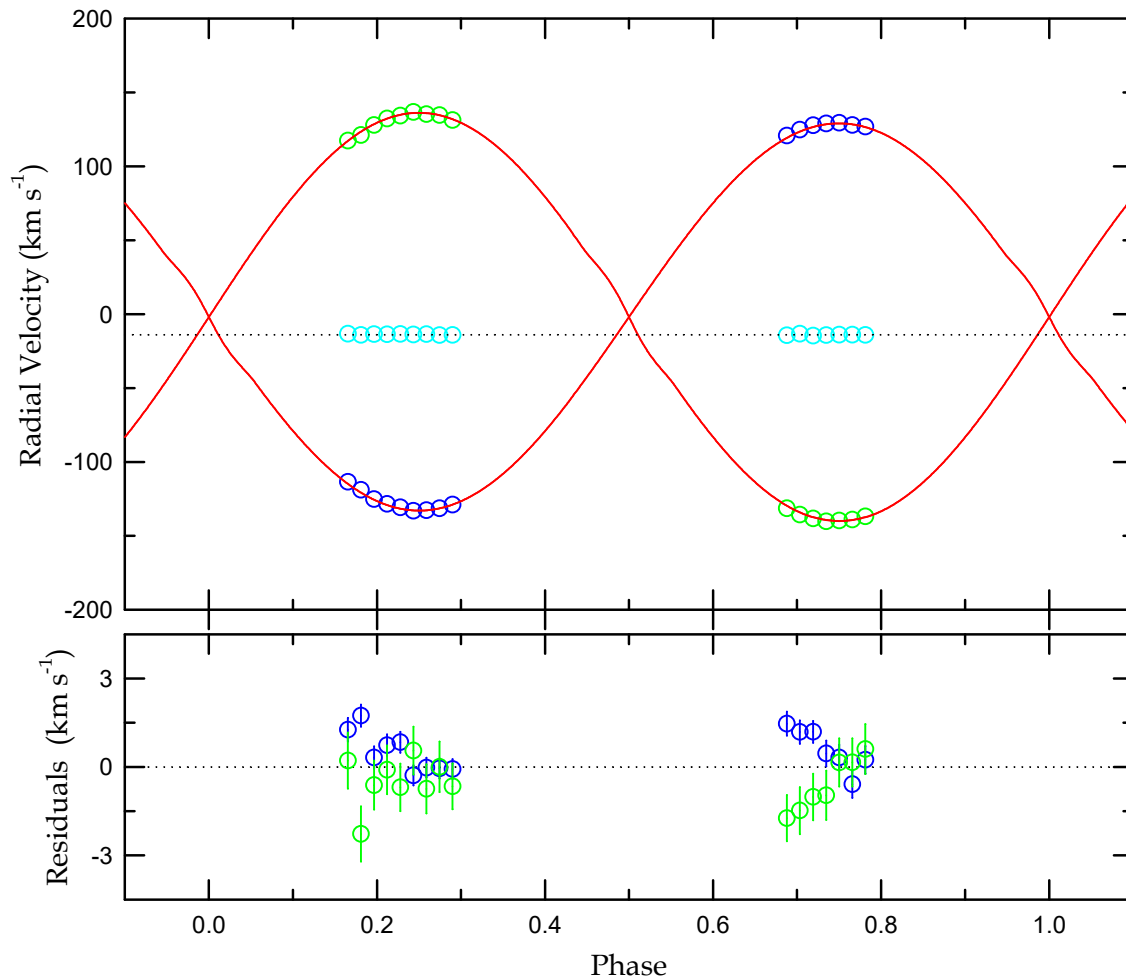


Figure 4. RV curves of TIC 322208686 with fitted models. The blue, green, and cyan circles are the RV measurements for the primary (A), secondary (B), and third (C) components, respectively. The red solid curves represent the results of the W-D binary model, and the dotted line denotes the average RV of -13.86 km s^{-1} for the third component. The lower panel shows the residuals between observations and models.

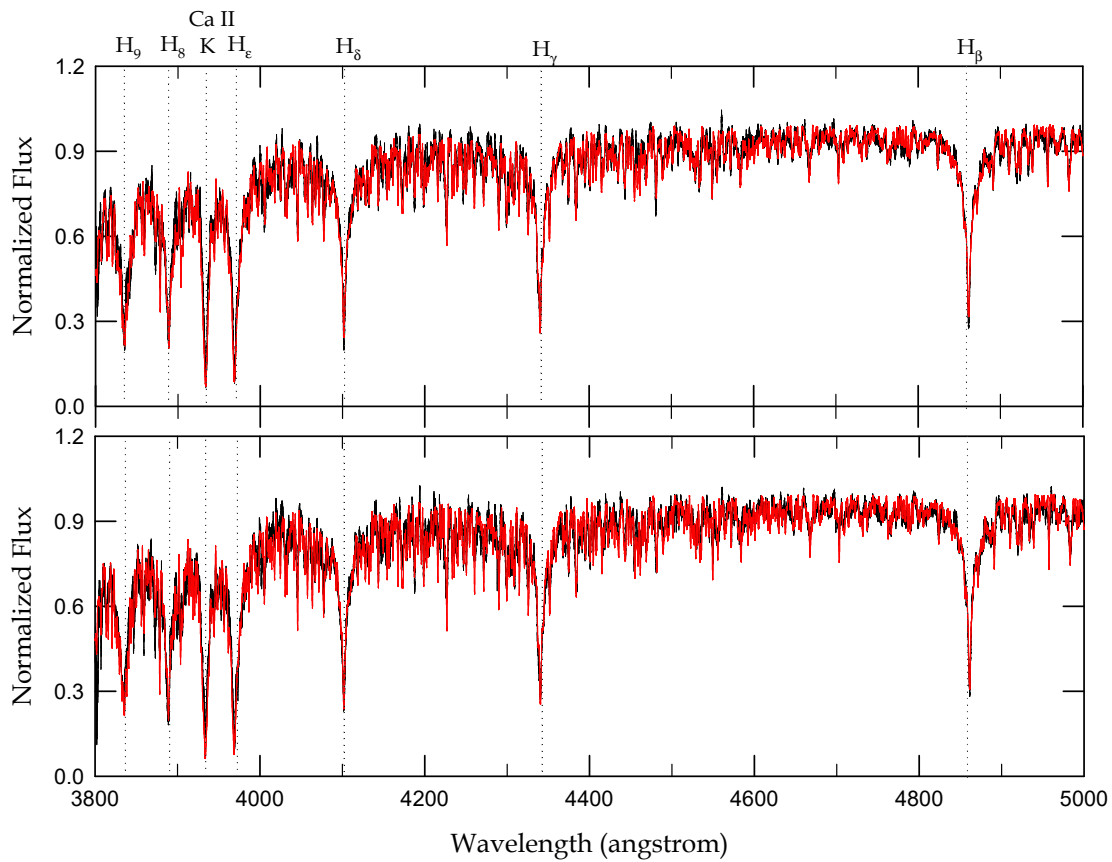


Figure 5. Disentangled spectra of the primary (upper panel) and secondary (lower panel) components for TIC 322208686. The black and red solid lines represent the disentangled and best-fitting synthetic spectra, respectively. The vertical dotted lines represent the spectral lines labeled above the upper panel.

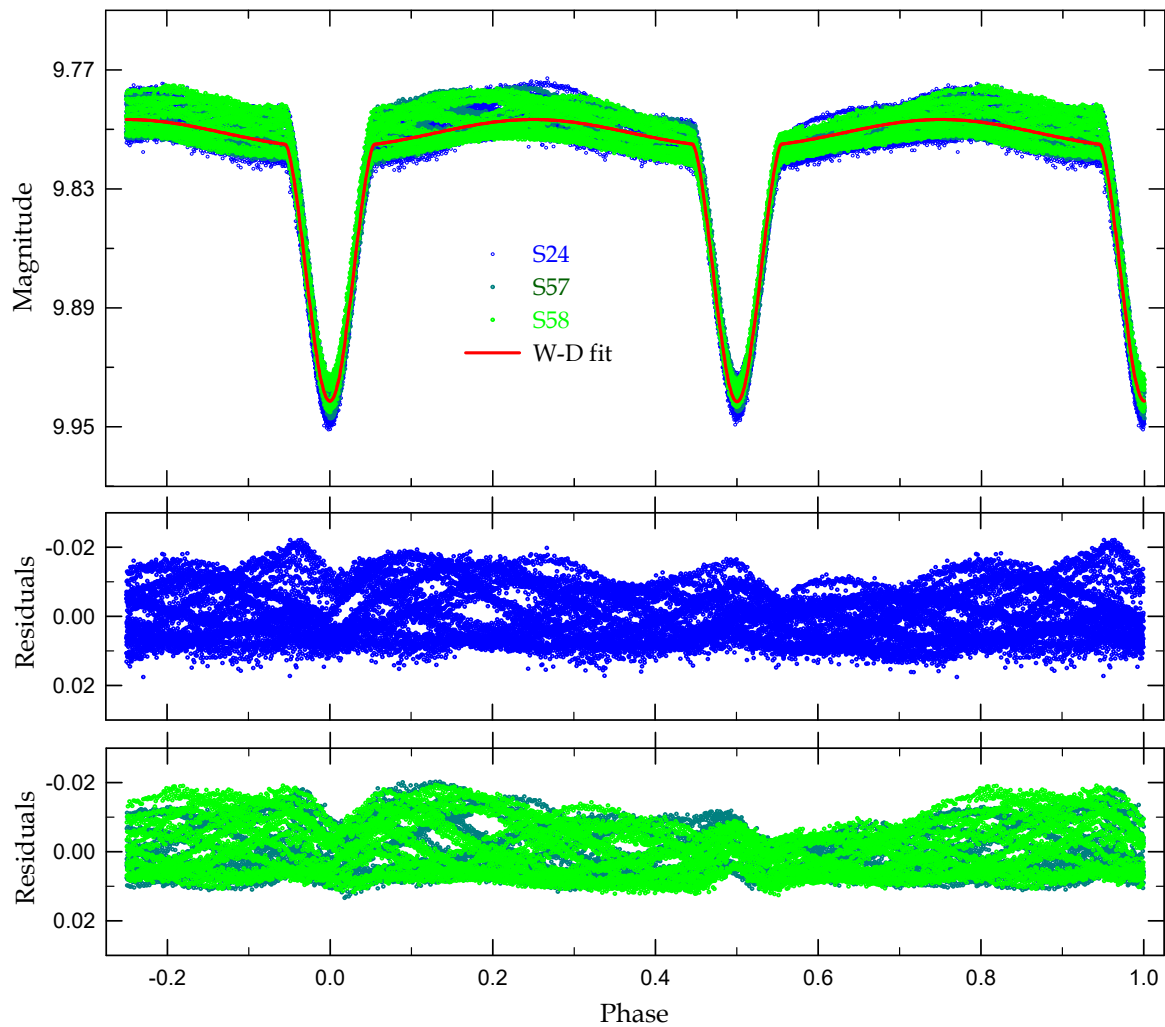


Figure 6. The top panel displays the phased light curve of TIC 322208686 with the fitted model. The blue, cyan, and green circles are the TESS measurements from Sectors 24, 57, and 58, respectively, and the red solid curve is computed with our W-D fit. The middle and bottom panels represent the corresponding residuals for 120-s and 200-s cadence data, respectively, from the synthetic curve.

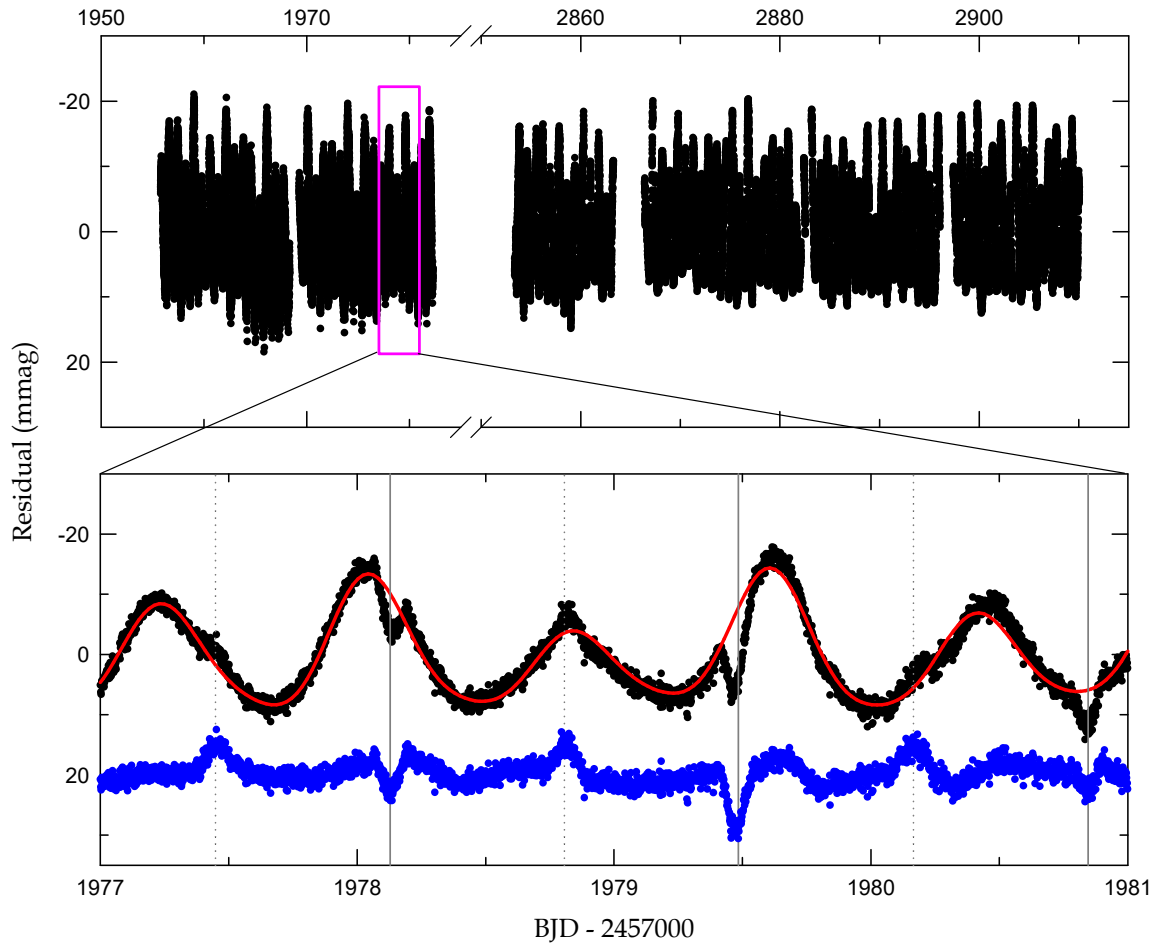


Figure 7. Light curve residuals from the W-D model fit to the TESS data. The lower panel is a zoomed-in view of the residuals shown in the inset box in the upper panel. The red solid line represents the synthetic curve computed from the 11-frequency fit to the out-of-eclipse data. The residuals from the frequency fit are offset from zero by +20 mmag for clarity and are plotted as the blue symbols. The vertical solid and dotted lines indicate the primary and secondary minimum epochs, respectively.

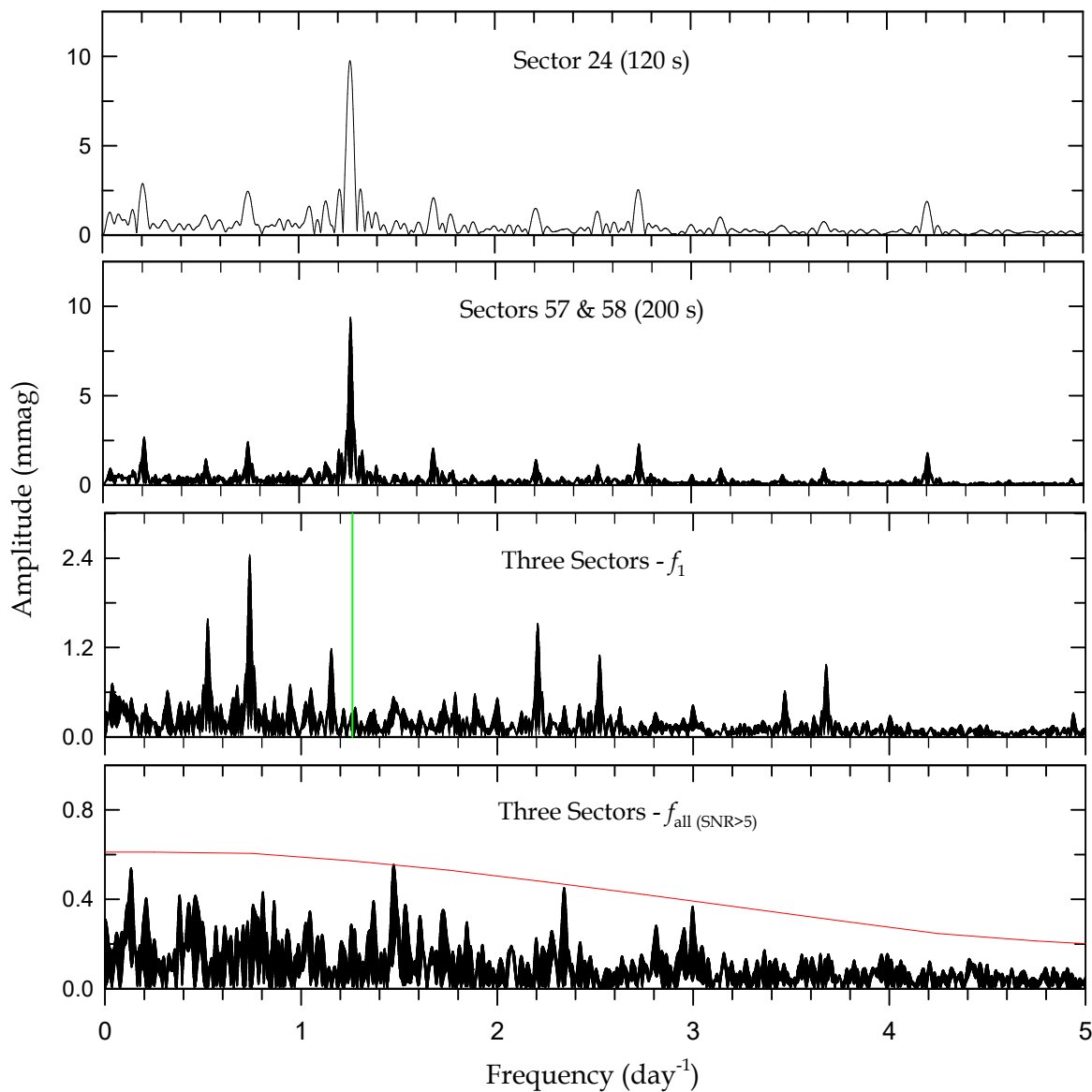


Figure 8. PERIOD04 periodograms for the outside-eclipse TESS residuals. The first and second panels show the amplitude spectra of the 120-s and 200-s residuals, respectively, while the third and bottom panels are obtained using the entire short-cadence data, pre-whitening the most dominant frequency (f_1) as indicated by a vertical green line and all 11 frequencies with $\text{SNR} > 5$, respectively. The red solid line in the bottom panel corresponds to five times the noise spectrum.

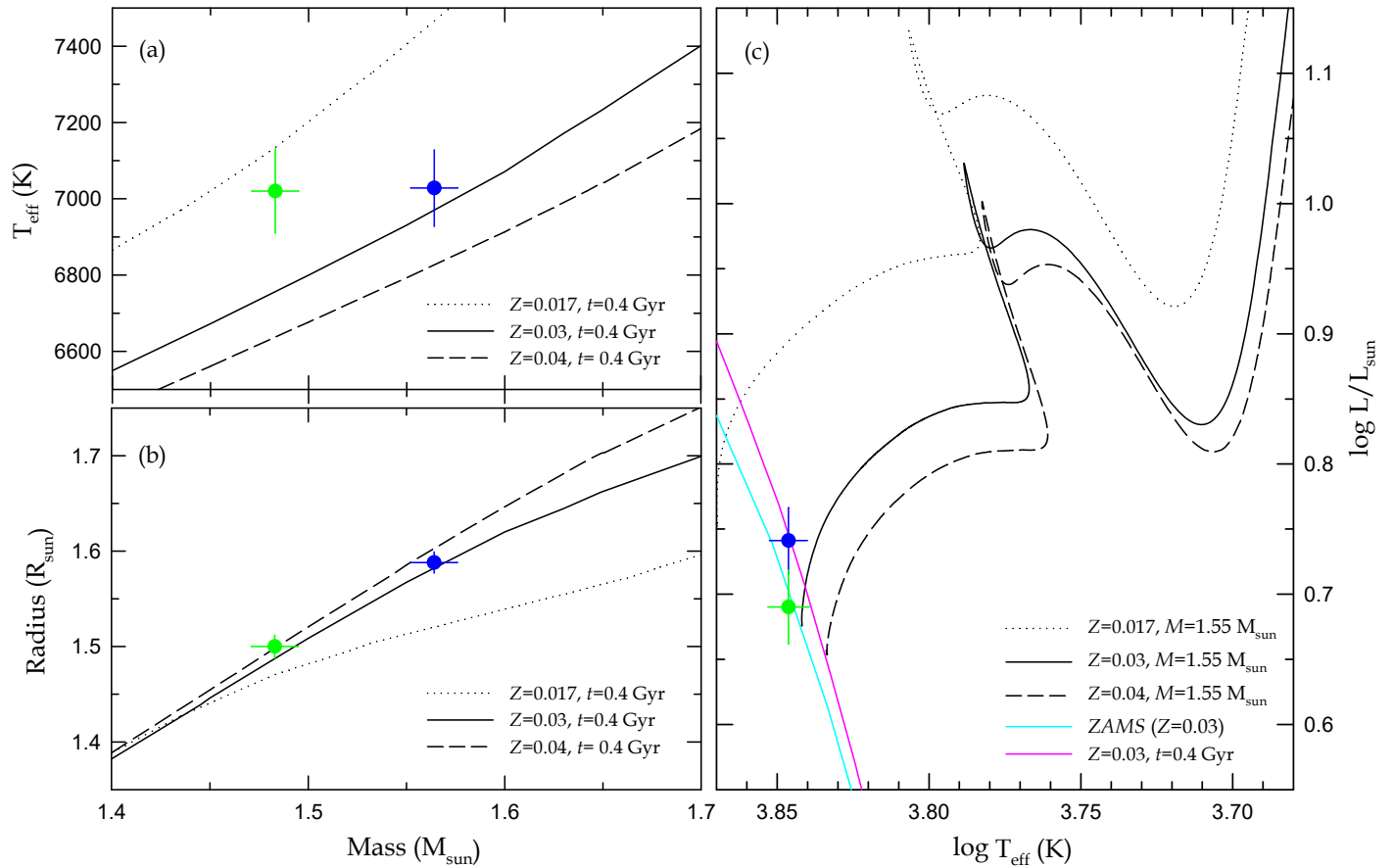


Figure 9. Position of TIC 322208686 A (blue circle) and B (green circle) on the mass-temperature (a), mass-radius (b), and H-R (c) diagrams. In all panels, the dotted, solid, and dashed lines are the theoretic predictions with different metallicities of $Z = 0.017$, 0.03 , and 0.04 , respectively, from the PARSEC models (A. Bressan et al. 2012). In the right panel, the ZAMS and 0.4-Gyr isochrone for $Z = 0.03$ are presented as cyan and red solid lines, respectively.

Table 1. TESS Eclipse Timings of TIC 322208686

BJD	Error	Epoch	$O - C$	Min
2,458,739.57378	± 0.00021	-159.5	+0.00230	II
2,458,740.25376	± 0.00036	-159.0	+0.00263	I
2,458,740.93124	± 0.00015	-158.5	+0.00045	II
2,458,741.61026	± 0.00068	-158.0	-0.00019	I
2,458,742.29154	± 0.00044	-157.5	+0.00144	II
2,458,742.97190	± 0.00025	-157.0	+0.00214	I
2,458,743.65167	± 0.00056	-156.5	+0.00225	II
2,458,745.01041	± 0.00038	-155.5	+0.00168	II
2,458,745.68781	± 0.00079	-155.0	-0.00058	I
2,458,746.36872	± 0.00015	-154.5	+0.00067	II

NOTE—This table is available in its entirety in machine-readable form. A portion is shown here for guidance regarding its form and content.

Table 2. Radial velocities of TIC 322208686[†]

BJD (2,460,000+)	V_A (km s ⁻¹)	σ_A (km s ⁻¹)	V_B (km s ⁻¹)	σ_B (km s ⁻¹)	V_C (km s ⁻¹)	σ_C (km s ⁻¹)
260.9055	+120.80	0.40	-131.29	0.79	-14.35	0.52
260.9267	+124.80	0.40	-135.57	0.80	-13.29	0.53
260.9479	+127.89	0.37	-138.38	0.79	-14.58	0.53
260.9690	+129.00	0.44	-140.30	0.84	-14.19	0.53
260.9902	+129.47	0.44	-139.84	0.82	-13.96	0.50
261.0114	+127.92	0.46	-139.18	0.82	-13.95	0.58
261.0326	+126.86	0.47	-136.75	0.85	-14.09	0.56
262.9139	-113.47	0.40	+117.50	0.95	-13.32	0.54
262.9350	-118.92	0.38	+121.26	0.94	-13.97	0.51
262.9562	-125.16	0.38	+127.99	0.83	-13.56	0.58
262.9774	-128.38	0.37	+132.33	0.83	-13.65	0.58
262.9986	-130.70	0.36	+134.27	0.80	-13.38	0.53
263.0198	-133.00	0.34	+136.74	0.81	-13.76	0.53
263.0409	-132.67	0.34	+135.36	0.84	-13.53	0.52
263.0621	-131.38	0.34	+134.68	0.86	-14.21	0.51
263.0833	-128.84	0.34	+131.30	0.77	-13.97	0.52

[†] V_A , V_B , and V_C represent the measured RVs of the primary, secondary, and third stars, respectively, and σ_A , σ_B , and σ_C are their uncertainties.

Table 3. Light and RV Parameters of TIC 322208686

Parameter	Primary (A)	Secondary (B)
T_0 (BJD)	2,458,956.37822±0.00030	
P_{orb} (day)	1.35931936±0.00000060	
i (deg)	75.40±0.16	
T_{eff} (K)	7028±100	7020±110
Ω	5.709±0.026	5.790±0.029
$\Omega_{\text{in}}^{\text{a}}$	3.666	
F	1.33±0.11	1.18±0.11
X, Y	0.640, 0.254	0.640, 0.253
x, y	0.527, 0.282	0.527, 0.282
$l/(l_{\text{A}} + l_{\text{B}} + l_3)$	0.4461±0.0049	0.3967
l_3^{b}	0.1572±0.0039	
r (pole)	0.2092±0.0013	0.1982±0.0015
r (point)	0.2163±0.0015	0.2037±0.0017
r (side)	0.2126±0.0014	0.2005±0.0016
r (back)	0.2153±0.0015	0.2029±0.0017
r (volume) ^c	0.2124±0.0014	0.2006±0.0016
Spectroscopic orbits:		
T_0 (BJD)	2,460,261.3299±0.0011	
a (R_{\odot})	7.483±0.019	
γ (km s^{-1})	−1.84±0.73	
K (km s^{-1})	131.24±0.45	138.39±0.46
q	0.9483±0.0045	

^aPotential for the inner critical Roche surface.

^bValue at 0.25 orbital phase.

^cMean volume radius.

Table 4. Absolute Parameters of TIC 322208686

Parameter	Primary (A)	Secondary (B)
$M (M_{\odot})$	1.564 ± 0.012	1.483 ± 0.012
$R (R_{\odot})$	1.588 ± 0.011	1.500 ± 0.012
$\log g$ (cgs)	4.230 ± 0.007	4.257 ± 0.008
$\rho (\rho_{\odot})$	0.391 ± 0.009	0.440 ± 0.011
v_{sync} (km s $^{-1}$)	59.11 ± 0.42	55.86 ± 0.47
$v \sin i$ (km s $^{-1}$)	76 ± 6	64 ± 6
T_{eff} (K)	7028 ± 100	7020 ± 110
$L (L_{\odot})$	5.51 ± 0.32	4.90 ± 0.32
M_{bol} (mag)	2.87 ± 0.06	3.00 ± 0.08
BC (mag)	0.03 ± 0.01	0.03 ± 0.01
M_V (mag)	2.84 ± 0.06	2.97 ± 0.08
$E(B - V)$ (mag)	0.054 ± 0.028	
Distance (pc)	323 ± 13	

Table 5. Multi-frequency Solution for TIC 322208686^{a,b}

	Frequency (day $^{-1}$)	Amplitude (mmag)	Phase (rad)	SNR ^c	Remark
f_1	1.26168 ± 0.00001	9.44 ± 0.20	2.83 ± 0.06	82.65	
f_2	0.73787 ± 0.00001	3.17 ± 0.21	2.95 ± 0.19	26.20	
f_3	0.52490 ± 0.00002	1.86 ± 0.21	3.84 ± 0.33	15.24	$f_1 - f_{\text{orb}}$
f_4	1.15402 ± 0.00003	1.26 ± 0.20	4.52 ± 0.46	10.88	
f_5	2.52335 ± 0.00003	1.10 ± 0.15	4.94 ± 0.41	12.26	$2f_1$
f_6	1.99951 ± 0.00004	0.82 ± 0.17	1.95 ± 0.62	8.09	$f_5 - f_3$
f_7	0.03486 ± 0.00006	0.75 ± 0.21	5.80 ± 0.82	6.10	artifact
f_8	0.65720 ± 0.00006	0.72 ± 0.21	5.52 ± 0.84	5.94	
f_9	1.78653 ± 0.00005	0.74 ± 0.18	3.93 ± 0.72	7.01	$f_1 + f_3$
f_{10}	0.07581 ± 0.00007	0.61 ± 0.21	3.63 ± 1.00	5.01	artifact
f_{11}	1.88617 ± 0.00006	0.58 ± 0.18	5.96 ± 0.90	5.59	

^aFrequencies are listed in order of detection.

^bParameters' errors were obtained following Kallinger et al. (2008).

^cCalculated in a range of 5 day $^{-1}$ around each frequency.